Check for updates

Solar RRL
www.solar-rrl.com

Laser Scribing for Perovskite Solar Modules of Long-Term Stability

Yujin Jeong, Yejin Kim, Hanseul Lee, Seoyeon Ko, Seung Sik Ham, Hye Ri Jung, Jun Hwan Choi, Won Mok Kim, Jeung-hyun Jeong, Seokhyun Yoon, David J. Hwang, and Gee Yeong Kim**

Although the efficiency of hybrid lead-halide perovskite solar cells has been significantly improved, the efficiency gap between small-area cells and large modules continues to be a considerable challenge. Laser scribing is essential for realizing high-quality monolithic connections; however, the laser-induced material changes and their correlation with device performance have not been yet well understood, in particular for the perovskite material systems. In this study, the effect of P3 laser processing conditions on device performance and stability is explained. The most interesting finding is an improvement in open-circuit voltage (V_{OC}) after aging and long-term stability under low-laser-overlap conditions that avoid direct laser exposure to perovskite material system as a source of material degradation. It is found that a high-laser-overlap during P3 results in a lower fill factor after aging and accelerated degradation due to larger portion of perovskite directly exposed to laser during the scribing process. The increased V_{OC} under low-overlap conditions is attributed to the increased PbI_2 formation in the P3 region. Moreover, a minimal pulse overlap is favorable for preserving long-term device stability. Finally, a perovskite minimodule with an efficiency of 20.24% is successfully developed as a result of these findings.

1. Introduction

Hybrid lead-halide perovskite solar cells (PSCs) are considered potential candidates for next-generation photovoltaics because of their advantages such as high efficiency, long charge-carrier lifetime, high absorption coefficient, tunable bandgap, and low-cost fabrication.[1] PSCs have received considerable research attention over the past decade because of these advantages. The state-of-the-art efficiency of PSCs is 26.1% in small area cells, which is over 19.54% in minimodules (@ 65 cm^2) and 18.6% (@ 809.9 cm^2) in small modules.[2,3] Currently, upscaling, modulation processes, and device stability are important aspects for the mass production and commercialization of PSCs.

So far, previous studies have reported various coating methods for large-area modules,[4–14] proper module designs,[15,16] and interconnection methods.[4,17–22] Also, monolithic interconnection plays a critical role in solar module performance, and therefore, interconnection methods such as mechanical scribing and laser scribing have been extensively studied.[17–21] Laser processing is widely used in various industrial applications because it offers a high throughput owing to its fast processing capabilities, and it can be employed in various applications, including flexible substrates, because it does not require direct-contact processing. Furthermore, laser scribing allows much narrower P1–P2–P3 lines compared to mechanical scribing with a knife, hence the dead area will be smaller. In this study, we used laser-scribing method due to its several advantages, including accuracy and fast processing.

Module interconnection was established as a serial connection using laser scribing and executed through P1, P2, and P3.[23,24] P1 and P3 separate adjacent cells by removing the bottom and top electrodes, respectively, and P2 exposes the bottom electrode to connect the top and bottom electrodes when the top-electrode material is deposited. The laser-scribing quality significantly

Y. Jeong, H. Lee, S. S. Ham, H. R. Jung, J. H. Choi, J. Jeong, G. Y. Kim
Advanced Photovoltaics Research Center
Korea Institute of Science and Technology
Seoul 02792, Korea
E-mail: gykim@kist.re.kr

Y. Jeong, H. Lee
Department of Material Science and Engineering
Korea University
Seoul 02841, Korea

The ORCID identification number(s) for the author(s) of this article can be found under https://doi.org/10.1002/solr.202301040.

DOI: 10.1002/solr.202301040

Y. Kim, S. Ko, S. Yoon
Department of Physics
Ewha Womans University
Seoul 03760, Korea

W. M. Kim
Electronic Materials Research Center
Korea Institute of Science and Technology
Seoul 02792, Korea

D. J. Hwang
Department of Mechanical Engineering
State University of New York
Stony Brook, NY 11794, USA
E-mail: david.hwang@stonybrook.edu

 © 2024 Wiley-VCH GmbH

affects the cell-to-module (CTM) loss.[25,26] So far, several researchers have reported on the mechanisms of the P1-, P2-, and P3-laser-scribing processes for perovskite modules and their effect on module performance.[20,27–31] Schultz et al. reported that picosecond (ps) laser scribing is suitable for P2 interconnects because of their steep edge shape and the low amount of PbI_2 remaining in the scribing area,[27] which leads to a poor fill factor (FF) because of the high series resistance.[27–29] Kosasih et al. investigated the effects of P3 scribing using laser- and mechanical-scribing methods[29] and observed that the ps-laser-scribing modified the perovskite composition near the P3 region. Further, they attributed the degradation of the perovskite to existing PbI_2 grains because of the preferential heat flow channel generated during ps laser heating, which anticipated even more pronounced laser-induced thermal damage when employing nanosecond (ns) lasers. Fenske et al. reported that performing P3 processing using an ns laser resulted in improved photovoltaic performance, such as higher open-circuit voltage (V_{oc}) and FF. This is due to the formation of PbI_2 in the P3 region and the creation of a Br-rich layer at the perovskite/HTL interface.[31] Meanwhile, other studies have shown that the formation of PbI_2 in PSCs acts as defect passivation, consequently enhancing the V_{oc} and FF of the devices.[32–34] These studies suggested that laser-scribing parameters and laser-induced material changes are significant in determining perovskite module efficiency. However, the effects of laser-scribing parameters on the device performance and stability are yet to be clarified. For example, the effect of P3-laser-scribing parameters, such as laser power and scanning speed, in correlation with the pulse overlap on the performance and long-term stability of perovskite modules requires further research. The device stability and performance should be monitored for an extended period because laser scribing directly exposes the edge of the active zone in an ambient air environment. Further, the P3 area should be minimized as part of the dead zone to reduce short-circuit current density (J_{SC}) loss.

In this study, we determined optimal P3-scribing conditions and their effects on device performance and long-term stability based on the power and scanning speed of the 532 nm ps laser. We aimed to reduce the CTM loss and achieve a high-efficiency module by minimizing edge delamination, inducing reactions via intermetallic diffusion, and causing junction damage by laser heating. To this end, we analyzed the morphology of the scribed area using optical microscopy (OM) and scanning electron microscopy (SEM). The selected P3-scribing conditions were applied at the cell level, and the current–voltage (J–V) characteristics were investigated before and after P3 processing. The V_{OC} and long-term stability improvements were observed at high scanning speeds (or low pulse overlap). We conducted photoluminescence (PL) mapping, transmission electron microscopy (TEM), and energy-dispersive X-ray spectroscopy (EDX) measurements to trace the origin of the V_{OC} improvement. The improved V_{OC} can be attributed to the large amount of PbI_2 formed in the P3-processed region under high-scanning-speed conditions. Additionally, a minimal pulse overlap is favorable for preserving long-term stability (tested up to ≈62 days in ambient air environment). Based on these findings, we fabricated a perovskite minimodule with a high-efficiency of 20.24%.

2. Result and Discussion

2.1. Fabrication Process of Base PSC

Figure 1a shows a schematic of the n–*i*–p structure (glass/Indium tin oxide (ITO)/SnO_2/(FA,MA)$Pb(I,Br)_3$/2,2′,7,7′-tetrakis-(N,N-di-p-methoxyphenyl-amine)-9,9′-spirobifluorene (Spiro-OMeTAD)/Au) PSC. In this study, Rb and MACl were employed as additives in the perovskite absorber layers. According to a previous study, the Rb additive increases charge-carrier mobility and reduces hysteresis in the J–V curve.[35–38] Further, the addition of MACl to a perovskite precursor improves light absorption by increasing the grain size.[31–33] Based on these methods, we obtained a base cell efficiency of 21.36%, J_{SC} of 24.18 mA cm^{-2}, V_{OC} of 1.12 V, and FF of 79.01% (Figure 1b) (**Table 1**).

2.2. P3 Scribing on PSC

Here, we focused on P3 scribing by selectively removing the Au layer for electrical isolation at the top-electrode level. The active

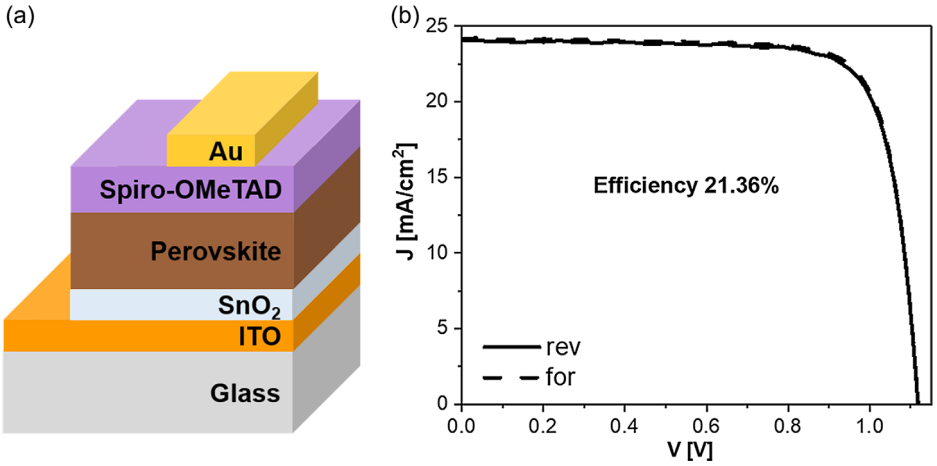


Figure 1. a) Schematic of the perovskite solar cell structure. b) J–V curve of the perovskite solar cell (active area of 0.07 cm^2).

© 2024 Wiley-VCH GmbH

2367198x, 2024, 8, Downloaded from https://onlinelibrary.wiley.com/doi/10.1002/solr.202301040 by Ewha Womans University Library, Wiley Online Library on [10/11/2024]. See the Terms and Conditions (https://onlinelibrary.wiley.com/terms-and-conditions) on Wiley Online Library for rules of use; OA articles are governed by the applicable Creative Commons License

Table 1. Device characteristics of the perovskite solar cell.

	V_{OC} [V]	J_{SC} [mA cm^{-2}]	FF [%]	Eff [%]
For	1.12	24.18	79.01	21.36
Rev	1.12	24.03	78.40	21.06

area was substantially damaged, and a large V_{OC} loss was observed in the perovskite modules when an inappropriate laser-scribing condition was applied to the upper electrode for the P3-scribing process (refer to next section). In previous work, we employed P3 scribing on copper indium gallium selenide (CIGS) solar cell with different power and overlap conditions. Under high-power and high-overlap conditions, substantial FF loss and 75% increase in dead zone were observed in CIGS solar cells.[39] Thus, it is important to minimize the P3-scribing width as part of the dead zone. A two-step P3-scribing mechanism is used for a single laser shot, which is schematically depicted in **Figure 2**a. 1) At the early stage, part of the irradiated ps laser pulse energy is absorbed on the top surface of the Au thin

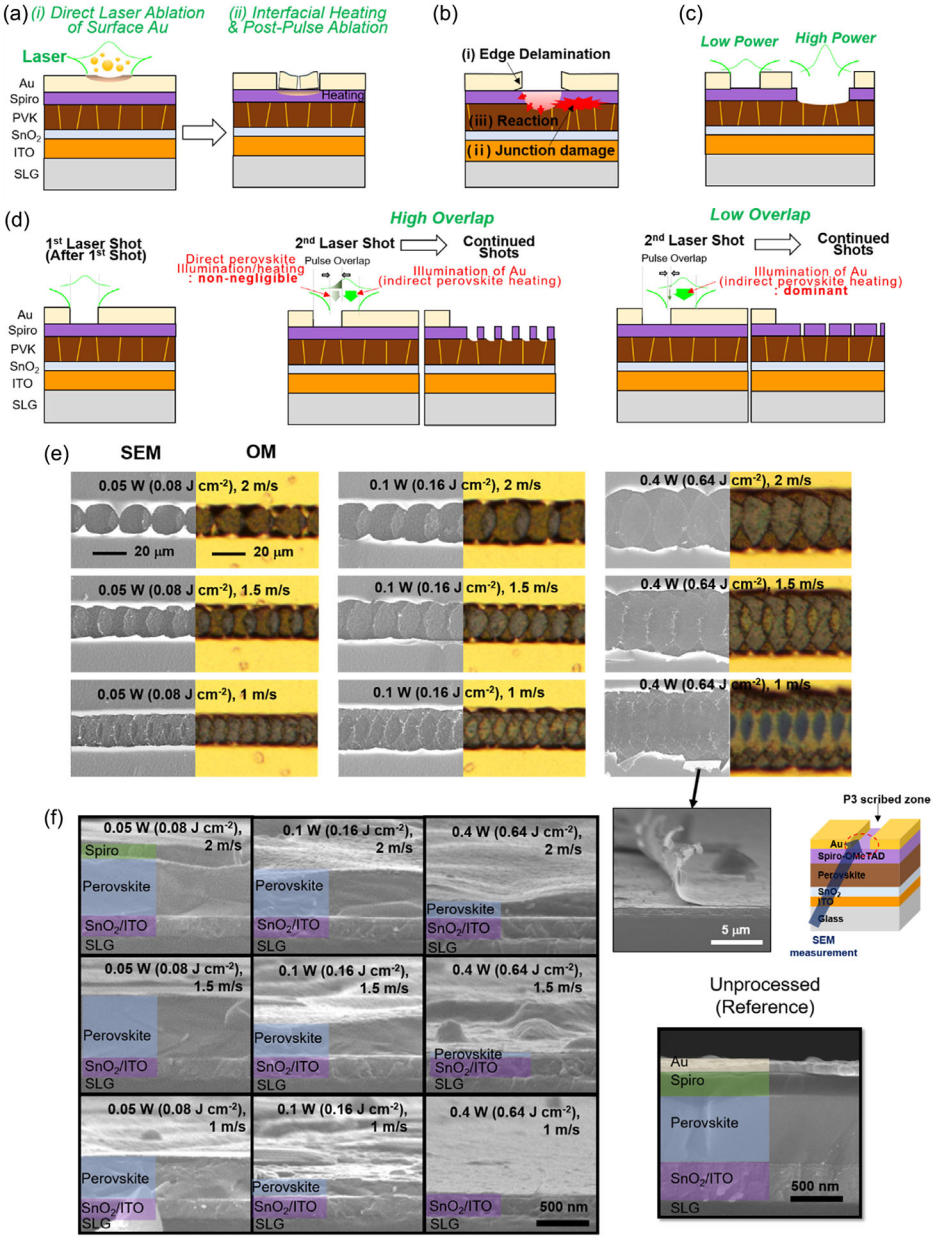


Figure 2. Schematic of a) the two-step P3-laser-scribing process: (left) direct laser ablation at the early stage followed by (right) post-pulse ablation attributed to the interfacial heating after thermal diffusion. b) P3-laser-scribing-induced damage mechanisms. c) P3-laser-scribing dependence on laser power. d) Practical-line-scribing mechanisms are schematically explained based on the pulse overlap. e) OM (reflection mode) and SEM images of P3-laser-scribed features are obtained by varying the laser power and scanning speed. f) Cross-sectional SEM images for the P3-laser-scribing central region cases in (e). The SEM images were taken in the direction perpendicular to the P3 line.

© 2024 Wiley-VCH GmbH

2367198x, 2024, 8, Downloaded from https://onlinelibrary.wiley.com/doi/10.1002/solr.202301040 by Ewha Womans University Library, Wiley Online Library on [10/11/2024]. See the Terms and Conditions (https://onlinelibrary.wiley.com/terms-and-conditions) on Wiley Online Library for rules of use; OA articles are governed by the applicable Creative Commons License

(≈20 nm linear absorption depth;[40] ps laser absorption in metallic sample still dominated by the single-photon absorption[41,42] thereby inducing direct ablative film removal within the pulse duration.[43,44] 2) At the later stage, heat is subsequently diffused to the Au-spiro/perovskite interface after the ps laser pulse terminates, thereby leading to Au film delamination via micro-explosion (triggered by the explosive phase change of spiro/perovskite[45,46]) or thermal stress mechanisms.[47,48]

Figure 2b schematically summarizes the possible issues involved with the single-shot P3-scribing process. Figure 2b shows that 1) the Au electrode delamination near the scribing edge depends on the adhesion of the Au electrode with the underlying layers as a source of the increased dead zone; 2) the diode is damaged by the laser-induced heating damage caused to the nip junction;[39,49] and 3) intermetallic diffusion between laser-heated layers and/or reactions with the ambient air environment (e.g., oxidation-induced material decomposition). A higher laser power (i.e., higher pulse energy) results in a larger scribing size laterally, and an increased scribing depth (removing more thickness/layers) is required for the given laser beam size (see Figure 2c). A series of ps laser pulses spatially overlap to form a continuous isolation line because of the complexity of the actual P3-scribing process. The scanning speed variation tunes the degree of the overlap between the laser pulses of the Gaussian spatial distribution, and therefore, it sensitively affects the scribing depth/layers for a fixed laser power (Figure 2d). Adjusting the laser power alters the effective pulse overlap with changes in the unit scribing size by an individual shot, which also affects the scribing depth/layers for a fixed-speed scanning.

Given this context, we examine a wide range of laser power levels (0.05–0.6 W; beam size: $13.6 \times 14.7\ \mu m^2$) and scanning speeds (1–2 m s^{-1} range) to explore the P3-line-scribing behavior. The OM and SEM results for the P3-scribing cases are summarized in Figure 2e. The OM and SEM images for a wider range of power variations are included in Figure S1 and S2, Supporting Information. The threshold laser power for ensuring electrical isolation in the Au top-electrode level is 0.05 W; 0.08 J cm^{-2}, and the laser power exceeding 0.6 W; 0.96 J cm^{-2} damages the bottom electrode. This is assumed to be an undesirable condition because such excessive power levels can disturb the surrounding material systems. As shown in the OM and SEM images in Figure 2e, the scribing threshold laser power of 0.05 W; 0.08 J cm^{-2} with the minimal pulse overlap, i.e., the case of the 2 m s^{-1} scanning speed, can achieve isolation across the scribing line at the top Au electrode level. The individual laser spots are clearly visible. We compared the surface OM images (Figure 2e) with the central region of the cross-sectional SEM images (Figure 2f). The brown-colored regions in the OM near the beam center location correspond to the exposed Spiro layer, and the gray regions at the pulse overlap sites are exposed to the perovskite layer, as confirmed by the cross-sectional SEM image in Figure 2f. A wider range of power variation and information about other colors are included in Figure S3, Supporting Information. The bright regions in the SEM image (Figure 2e) indicate a deformed Au film near the scribing edge, whereas these regions appear dark in the reflected OM image. The use of the threshold laser power at minimal overlap represents the safest condition in terms of minimal impact on the surrounding material systems. We distinguished the material remaining after P3 from the color in the OM image by comparing the surface and cross-sectional images (Figure S4 and S5, Supporting Information).

An increased pulse overlap causes the scribed Au edges to become smoother with more stable isolation; however, the spiro layer removal becomes prominent at 1.5 m s^{-1} and a significant thickness portion of the perovskite is removed at 1 m s^{-1} at the increased pulse overlap sites (Figure 2e,f). As schematically explained in Figure 2d, in the P3-scribing process that relies on an increased pulse overlap, each laser pulse tends to illuminate/remove a smaller arc fraction of the Au film. The remaining portion of the laser beam directly illuminates and increasingly removes the preexposed spiro/perovskite layer. Given the spatially Gaussian laser beam profile, the preexposed spiro/perovskite layer is subjected to a considerably higher laser intensity through an enlarged Gaussian tail region (the minimal overlap is safe because of the low laser intensity involved) with an increase in the pulse overlap, which can cause different types of risks. A possible issue is that the perovskite layer exposed to ambient air may be degraded by oxygen- or moisture-induced reactions. Another concern is that the 532 nm ps laser will penetrate deeply into the perovskite (spiro is transparent to 532 nm wavelength) if it is directly illuminated onto the spiro/perovskite without being screened by the Au film, possibly leading to significant damage/degradation of the perovskite material systems.

Figure 2e,f shows that a higher laser power leads to a larger scribing width with deeper spiro/perovskite removal at enlarged effective overlap sites at a given scanning speed. The areal fraction of the spiro-covered zone shrinks rapidly with an increase in the laser to 0.1 and 0.4 W (0.16 and 0.64 J cm^{-2}) at a scanning speed of 2 m s^{-1}. Further, perovskite removal is unavoidable near the scribing center at the elevated laser power conditions, which is caused by the indirect heating of perovskite by the diffused (conducted) heat from the laser illuminated Au film. The higher thickness of perovskite is removed gradually until SnO_2/ITO is exposed when the scanning speed reduces to 1.5 and 1 m s^{-1}, which can be attributed to the direct laser illumination of the preexposed spiro/perovskite under high-overlap conditions. A large pulse overlap, especially with a higher laser power, shows unacceptable Au delamination behavior at the scribing edge (shown in the SEM images with tilted view in the inset for 0.4 W; 0.64 J cm^{-2} laser power and 1 m s^{-1} scanning speed). It is mentioned that we have tested with the laser power lower than single-shot scribing threshold (<0.05 W) and lower scanning speed (<1 m s^{-1}) (see Figure S6a, Supporting Information) expecting scribing conditions with reduced thermal effect. However, power levels below the single-shot threshold didn't allow the full electrical isolation, and in general scanning speeds lower than 1 m s^{-1} resulted in excessive deformation of Au in the scribing edge. We have also tested with enlarged laser beam (by defocusing laser beam on sample surface, see Figure S6b, Supporting Information), however, the resulting features were wider (larger dead zone) with a prominent trend of Au delamination at the scribing edge leading to higher device loss with potentially higher risk in terms of device stability. As long as electrical isolation is achievable, a threshold laser power with minimal pulse overlap is favorable for preserving long-term device stability during the module fabrication process.

© 2024 Wiley-VCH GmbH

2367198x, 2024, 8, Downloaded from https://onlinelibrary.wiley.com/doi/10.1002/solr.202301040 by Ewha Womans University Library, Wiley Online Library on [10/11/2024]. See the Terms and Conditions (https://onlinelibrary.wiley.com/terms-and-conditions) on Wiley Online Library for rules of use; OA articles are governed by the applicable Creative Commons License

However, we performed *J–V* characterization because the effects of the increased laser power and/or pulse overlap are difficult to predict.

2.3. P3-Scribing test on PSC

We measured the *J–V* characteristics of the PSCs before and after P3 scribing to examine the P3-laser-scribing-induced efficiency loss and/or degradation in PSCs. As shown in **Figure 3**a, a short-P3-scribing line was drawn within a small electrically isolated cell area. Then, it measured the corresponding *J–V* curves as representative results (see Figure 3 and **Table 2**).

Figure 3b shows the measured *J–V* characteristics before and after P3 scribing at a laser power of 0.05 W (0.08 J cm^{-2}) with scanning speeds of 1 and 2 m s^{-1}. Minor FF losses were detected immediately after P3 scribing; however, no significant changes were observed in V_{OC} or J_{SC}. The FF was obviously recovered for the low pulse overlap case (scanning speed of 2 m s^{-1}) after 62 days of aging in a dark ambient air environment at room temperature, and interestingly, the V_{OC} increased by ≈3%. In contrast, for the high-overlap case (scanning speed of 1 m s^{-1}), FF, J_{SC}, and V_{OC} experienced significant losses after 62 days of aging.

The two possible issues with the high-pulse-overlap operation by near-scribing the threshold laser power (0.05 W; 0.08 J cm^{-2}) as the potential source of perovskite degradation include 1) a lack of a spiro layer as a shield for the perovskite reaction in ambient air and 2) a deep penetration of the directly illuminated 532 nm ps laser beam onto the perovskite (thermal damage). The *J–V* characteristics at a higher laser power (0.4 W; 0.64 J cm^{-2} are shown in Figure 3c), and Table 2 provides further details. Interestingly, the dependence of *J–V* characteristics on the scanning speed and long-term stability was similar, regardless of the laser power within the scope of the current study. The low-pulse-overlap condition (2 m s^{-1}) maintains long-term efficiency even for an order of magnitude higher laser power despite the spiro removal over a significantly larger fraction of the scribed area (Figure 2e), which supports the dominance of the latter mechanism. A deep penetration of the directly illuminated green ps laser is the main source of perovskite thermal degradation considering the extreme intensity of the ps laser beam even at the Gaussian tail.

Figure 3d summarizes the *J–V* curves after 62 days of aging for scanning speeds of 1, 1.5, and 2 m s^{-1} for laser powers of 0.05, 0.2, and 0.4 W, respectively (the *J–V* curve after aging for 62 days at 0.05 W; 0.08 J cm^{-2} and 0.4 W; 0.64 J cm^{-2}, and

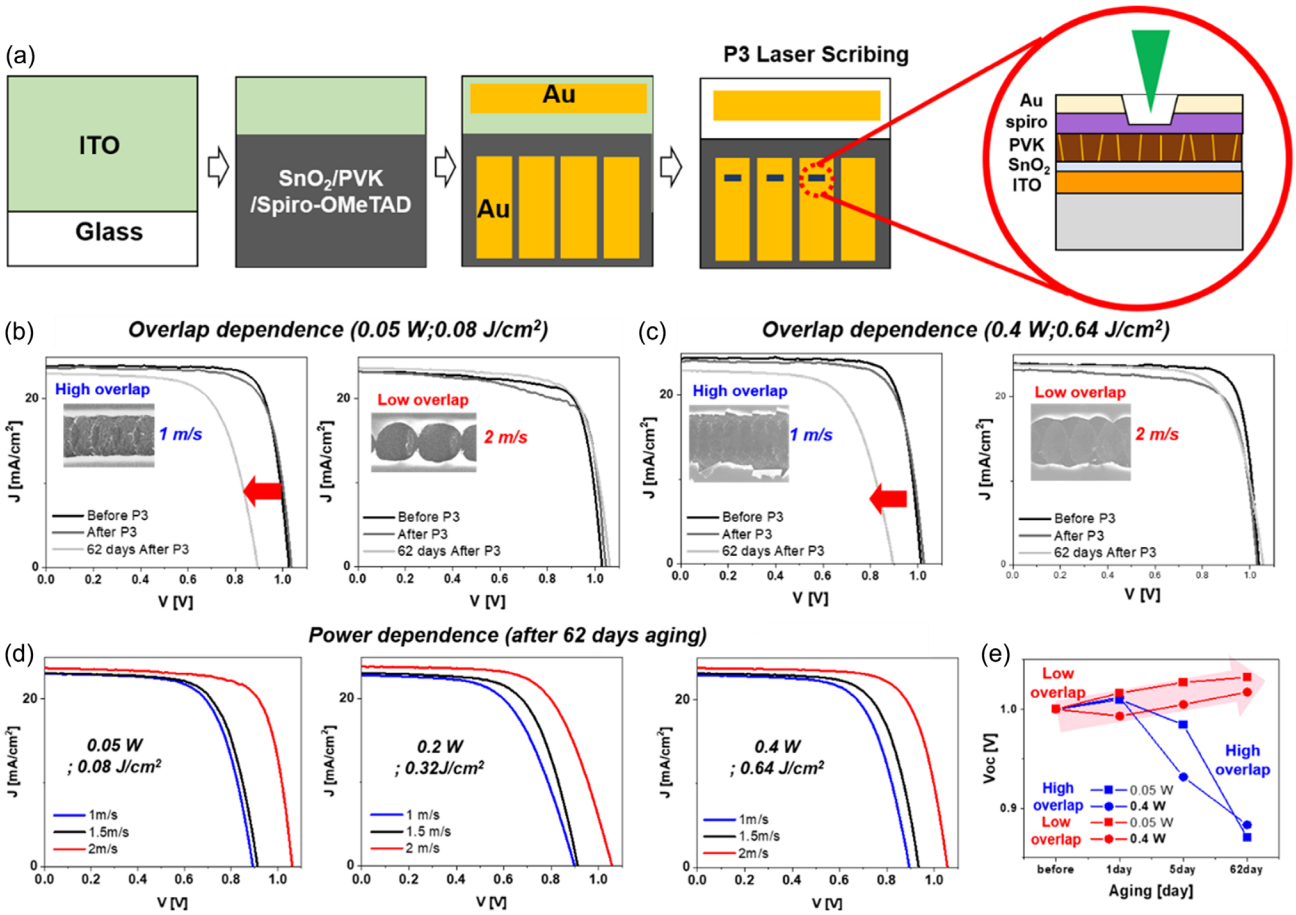


Figure 3. a) Schematic of the P3-scribing test. *J–V* curves before and after P3 scribing using b) a 0.05 W; 0.08 J cm^{-2} and c) 0.4 W; 0.64 J cm^{-2} laser power at scanning speeds of 1 and 2 m s^{-1}. d) *J–V* curves after 62 days of aging in a dark ambient air environment by 0.05 W; 0.08 J cm^{-2}, 0.1 W; 0.32 J cm^{-2}, and 0.4 W; 0.64 J cm^{-2} for 1, 1.5, and 2 m s^{-1}. e) V_{OC} variation per aging time for different laser-power and pulse-overlap conditions (low overlap—2 m s^{-1}, high overlap—1 m s^{-1}).

© 2024 Wiley-VCH GmbH

2367198x, 2024, 8, Downloaded from https://onlinelibrary.wiley.com/doi/10.1002/solr.202301040 by Ewha Womans University Library, Wiley Online Library on [10/11/2024]. See the Terms and Conditions (https://onlinelibrary.wiley.com/terms-and-conditions) on Wiley Online Library for rules of use; OA articles are governed by the applicable Creative Commons License

Table 2. Device characteristics of P3-scribing test for perovskite solar cells under different laser power and scanning speed conditions.

Power	Scanning speed (overlap)		V_{OC} [V]	J_{SC} [mA cm^{-2}]	FF [%]	Eff [%]
0.05 W (0.08 J cm^{-2})	1 m s^{-1} (high)	Before	1.03	23.95	79.61	19.56
		After	1.04	23.77	76.02	18.72
		After 62 days	0.89	23.03	67.02	13.78
	1.5 m s^{-1} (mid)	Before	1.03	23.91	81.39	19.94
		After	1.04	23.67	79.55	19.51
		After 62 days	0.91	23.1	68.07	14.37
	2 m s^{-1} (low)	Before	1.03	23.21	77.85	18.6
		After	1.05	23.25	75.97	18.48
		After 62 days	1.06	23.69	73.98	18.61
0.2 W (0.32 J cm^{-2})	1 m s^{-1} (high)	Before	1.01	24.45	79.64	19.72
		After	1.04	24.07	76.47	19.13
		After 62 days	0.9	22.82	58.46	12
	1.5 m s^{-1} (mid)	Before	1.01	24.28	81.5	20
		After	1.03	23.84	77.43	19.05
		After 62 days	0.91	23.07	64.13	13.49
	2 m s^{-1} (low)	Before	1.03	23.78	80.67	19.73
		After	1.04	23.2	77.10	18.54
		After 62 days	1.06	23.84	63.80	16.08
0.4 W (0.64 J cm^{-2})	1 m s^{-1} (high)	Before	1.01	24.38	79.91	19.72
		After	1.02	24.05	76.23	18.78
		After 62 days	0.89	22.93	65.71	13.47
	1.5 m^{-1} (mid)	Before	1.01	24.4	80.44	19.90
		After	1.03	23.98	76.95	18.94
		After 62 days	0.93	23.17	68.07	14.73
	2 m s^{-1} (low)	Before	1.04	23.94	80.88	20.08
		After	1.03	23.23	74.14	17.74
		After 62 days	1.06	23.79	71.47	17.94

the cell without P3 processing are shown in Figure S7, Supporting Information). A noticeable decrease in V_{OC} is observed under the high-overlap conditions of 1 and 1.5 m s^{-1}. A slight decrease in FF is observed under the minimal-pulse-overlap condition of 2 m s^{-1}, whereas the V_{OC} is maintained without a decrease after the aging step. This trend is similarly observed over a wider range of laser powers and speeds (refer to Figure S8, Supporting Information, to check the J–V curves for a full range of laser powers: 0.05, 0.1, 0.2, 0.4, and 0.6 W, and for scanning speeds of 1, 1.5, and 2 m s^{-1}). The existence of a wide processing window in terms of laser power is favorable, and stable electrical isolation can be achieved by the minimal pulse overlap with a laser power above the threshold. Figure 3e shows that the long-term degradation/recovery is dictated by V_{OC}. PL and cross-sectional TEM analysis results adjacent to the P3 region are presented to further understand the laser-induced changes.

In terms of the efficiency drop measured right after P3 scribing versus before P3 scribing, we can observe weak dependences on the power and scanning speed, i.e., both higher power and higher pulse overlap tends to induce more of efficiency drop, possibly related to higher scribing depth (refer to Figure 2, S3, and S4, Supporting Information) and/or larger mechanical/thermal impact on the surrounding perovskite material system. However, the long-term stability judged by the efficiency drop after ≈2 months versus right after P3 scribing, is predominantly dictated by pulse overlap (i.e., degree of direct laser exposure to perovskite) rather than laser power (i.e., etch depth or layers exposed).

This finding just described provides important practical clues to the optimal P3-scribing parameters for the tested perovskite structures, i.e., although the low pulse overlap operation with near the threshold laser power is considered to be the condition allowing the minimal thermal impact with enhanced long-term stability, it may suffer from incomplete electrical isolation. One possible solution is the multiple line scan approach with an appropriate overlap so that electrical isolation is secured with the minimal thermal effect, however at the expense of module efficiency due to increased scribing width (i.e., dead zone). Although one might think that multiple scans without offset relying on the threshold power would be a possible solution, it is logical prediction that such a repeated direct laser illumination

© 2024 Wiley-VCH GmbH

2367198x, 2024, 8, Downloaded from https://onlinelibrary.wiley.com/doi/10.1002/solr.202301040 by Ewha Womans University Library, Wiley Online Library on [10/11/2024]. See the Terms and Conditions (https://onlinelibrary.wiley.com/terms-and-conditions) on Wiley Online Library for rules of use; OA articles are governed by the applicable Creative Commons License

onto partially exposed perovskite would worsen the long-term stability as well as and affect module performance.[31]

Note that previously we investigated laser scribing using a similar approach not only for perovskites but also for CIGS.[39] For P2 scribing, excessive overlap led to damage in the bottom electrode of the lower layer and the flexible substrate. If the overlap is too small, material removal is not properly achieved, so low-overlap conditions within an appropriate range are suitable for P2 scribing. This approach is relevant to a broad range of optimum pulse-to-pulse overlap application. Additionally, we also tested P3 scribing with different power and overlap conditions on CIGS solar cells. The results showed that there was a loss of efficiency in the high power and high-overlap conditions compared to the low-overlap condition. To demonstrate broad applicability, we are conducting P3-scribing tests on inverted PSCs and modules. Details of these effects will be investigated in the future.

2.4. Investigation of Laser-Induced Effect: PbI_2 Passivation

We performed PL, cross-sectional TEM, and EDX measurements to trace the origin of V_{OC} enhancement and the laser-induced material changes. **Figure 4**a–d shows the cross-sectional TEM and EDX mapping results at the P3-scribed regions under different laser powers and overlap conditions. The green region in the TEM image represents the residual material after P3 scribing.

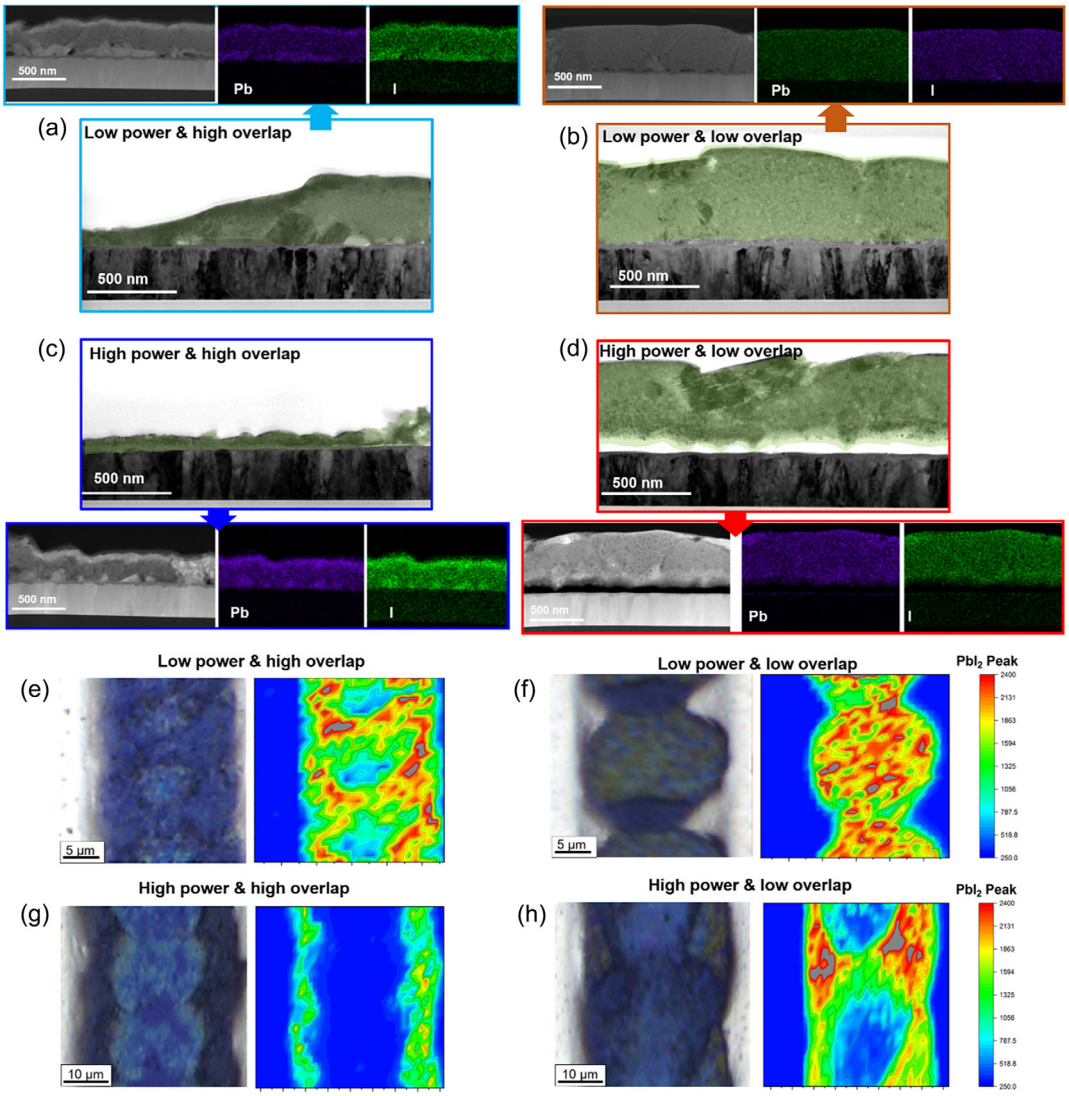


Figure 4. a–d) Cross-sectional TEM and EDS mapping (Pb, I) images of perovskite modules after P3 scribing (aged samples) according to different laser powers and scanning speeds. The conditions are as follow: a) 0.05 W; 0.08 J cm^{-2} and 1 m s^{-1}; b) 0.05 W; 0.08 J cm^{-2} and 2 m s^{-1}; c) 0.4 W; 0.64 J cm^{-2} and 1 m s^{-1}; and d) 0.4 W; 0.64 J cm^{-2} and 2 m s^{-1}. We measured TEM in the area of adjacent to the P3-scribed region: a) image of the central-edge area and b–d) images of the central regions of P3 (see the OM images marked with a red box in Figure S15, Supporting Information). The TEM images were taken in the direction perpendicular to the P3 line. e–h) Optical microscopy and PL mapping images of P3-scribed region according to different laser powers and scanning speeds. The PL measurement conditions are as follow: laser power 0.01 mW, mapping at 457 nm, exposure time 50 ms, and average size of mapping area 40 × 30 μm^2. Inset image in (b), accidental delamination between ITO and perovskite layers occurs during FIB.

© 2024 Wiley-VCH GmbH

2367198x, 2024, 8, Downloaded from https://onlinelibrary.wiley.com/doi/10.1002/solr.202301040 by Ewha Womans University Library, Wiley Online Library on [10/11/2024]. See the Terms and Conditions (https://onlinelibrary.wiley.com/terms-and-conditions) on Wiley Online Library for rules of use; OA articles are governed by the applicable Creative Commons License

The Gaussian beam energy causes more materials to be removed in the central region (Gaussian central region) of the P3 line than at the edges (Gaussian edge region) when the laser beams overlap. Therefore, the overall thickness of the center is less than that of the edge, as shown in Figure 4a.

As shown in Figure 4c, , a substantial portion of the perovskite layer is removed, leaving only a small residual amount of perovskite under high-power and high-overlap conditions. The elemental mapping results (Figure 4a,c) show that the whitish particles are PbI_x-related compounds. The PbI_x-related grains formed at the top and bottom of the film under high-overlap conditions; however, the perovskite and HTL layers remain intact when using low-overlap and low-power conditions. Only Au is removed in the area where the laser does not overlap as shown in Figure 2f and the spiro-OMeTAD is partially removed in localized areas where the laser is overlapped. Under high-power and low-overlap conditions, the HTL layer is removed and the perovskite layer is partially eliminated (Figure 4d). This result is consistent with our expectations presented in Figure 2d. The PbI_x compound was formed only on the surface of the film under low-overlap conditions.

We performed the PL mapping of the processed area under different laser-scribing conditions to determine whether the formed PbI_x compound is PbI_2 and whether the formation of PbI_x is due to material aging or laser-induced material changes. Further, we discuss the origin of V_{OC} enhancement effect after P3 scribing in PSCs. We selected a 457 nm laser to observe the PbI_2 spectrum using PL measurements. The PL emission is detected at ≈780 and 475 nm, corresponding to the perovskite and PbI_2 signals, respectively (Figure S9, Supporting Information). From this experiment, we derive the observed PbIx compound is PbI_2. As shown in Figure 4e–h, we obtain PL mapping images of the PbI_2 peak on the aged samples with different laser powers and overlap conditions. Strong PbI_2 emission was displayed in the scribed region under low-overlap and low-power conditions. However, the high-power and high-overlap conditions resulted in weak PbI_2 emission around the P3-scribing region. The reason for the low amount of PbI_2 under high-overlap conditions may be that a significant portion of the perovskite was removed, which resulted in a low absolute amount of PbI_2. Under these conditions, residual PbI_2 is formed by laser-induced material changes rather than material aging. To support this explanation, we compared the PL mapping data of the P3-scribing areas before and after aging to determine whether the PbI_2 formation was caused by laser-induced material changes or material aging (see Figure S10, Supporting Information). According to the PL results, there is no substantial increase in PbI_2 formation before and after 1 month of aging under high-overlap and high-power conditions (Figure S10a, Supporting Information). Therefore, we can consider that PbI_2 formation is not provided by material aging but rather by laser-induced material changes. The poor stability under high-overlap conditions is attributed to direct perovskite heating by the laser beam and extensive exposure to ambient conditions. For the low-overlap conditions, we observe a higher amount of PbI_2 not only at the center but also at the edge of the scribed area when the sample is aged (Figure S10b, Supporting Information). The PL mapping results indicated that there is a small amount of PbI_2 before aging; however, the amount of PbI_2 significantly increases after one month of aging (Figure S10, Supporting Information). Therefore, the presence of a large amount of PbI_2 under low-overlap conditions can be attributed to the decomposed phase resulting from more residual perovskite after aging rather than the laser-induced material changes. This result indicates that the smaller the laser overlap, the more PbI_2 are formed in the scribing region, which, in turn, plays a role in passivating the region in contact with the active area and improving V_{OC} and the low FF loss of the device. Therefore, it is reasonable to assume a correlation between the presence of PbI_2 and the enhancement of V_{OC}.[31,33,50,51] Additionally, we have investigated the effect of PbI_2 in our PSCs by adding a PbI_2 passivation layer between the perovskite and SnO_2 layer as well as using a PbI_2 additive. The result showed that there is a slight improvement in efficiency (see Figure S11, Supporting Information). Meanwhile, several studies suggested that excess PbI_2 leads to rapid degradation and has detrimental effects on the long-term stability of perovskite devices.[52,53] These interpretations are expected to vary depending on 1) the structure of the perovskite device, 2) exact distribution and quantity of PbI_2, 3) existence of Pb–I-related compounds, 4) aging state, and 5) impurity and defect concentrations of PbI_2. Nevertheless, PbI_2 formed in PSCs (especially at low-overlap conditions) did not cause rapid degradation in this study.

Figure S12 and S13, Supporting Information, show the position dependence of the PL spectra (PbI_2 peak) of the processed samples. The change in the PbI_2 PL spectra of different parts of a sample can be indicative of the different thicknesses of PbI_2 in the P3-scribed region. The PL energy of the PbI_2 depends on the thickness of PbI_2 and the PL peak shifts in relation to the number of PbI_2 layers.[54] A previous study suggested a change in the bandgap between bulk (≈2.3 eV) and thin layer configurations (≈2.6 eV).[55] Thus, the measured PL peak of PbI_2 shifts (blue) as its thickness decreases. The different PbI_2 PL peak positions indicate that the formed thickness of the PbI_2 in the laser-scribed region differs depending on the laser-scribing parameters (the entire PL spectrum including perovskite and PbI_2 can be seen on Figure S14, Supporting Information).

2.5. Characterization at a Monolithic Integrated Perovskite Module Level

We fabricated monolithic integrated perovskite modules to confirm the optimal P3-scribing parameters at the minimodule level, using the fabrication steps schematically shown in **Figure 5**a. The equivalent circuit of the minimodule is shown in Figure 5b. The coating methods for each layer of the perovskite solar modules were identical to those for the cell-level testing described earlier. However, the respective P1-, P2-, and P3-laser-scribing tasks were inserted at the corresponding steps. The details of the laser-scribing process are as follows.

1) P1–P1 selectively removes ITO for the electrical isolation at the bottom electrode level. An important aspect of P1 laser scribing is minimizing the melting-induced ridge formation at the scribing edge, which corresponds to the major source of shunts, especially for thin perovskite material systems. In this study, we relied on ns laser pulses with a wavelength of 532 nm to invoke the thermal-stress-assisted removal of relatively

© 2024 Wiley-VCH GmbH

2367198x, 2024, 8, Downloaded from https://onlinelibrary.wiley.com/doi/10.1002/solr.202301040 by Ewha Womans University Library, Wiley Online Library on [10/11/2024]. See the Terms and Conditions (https://onlinelibrary.wiley.com/terms-and-conditions) on Wiley Online Library for rules of use; OA articles are governed by the applicable Creative Commons License

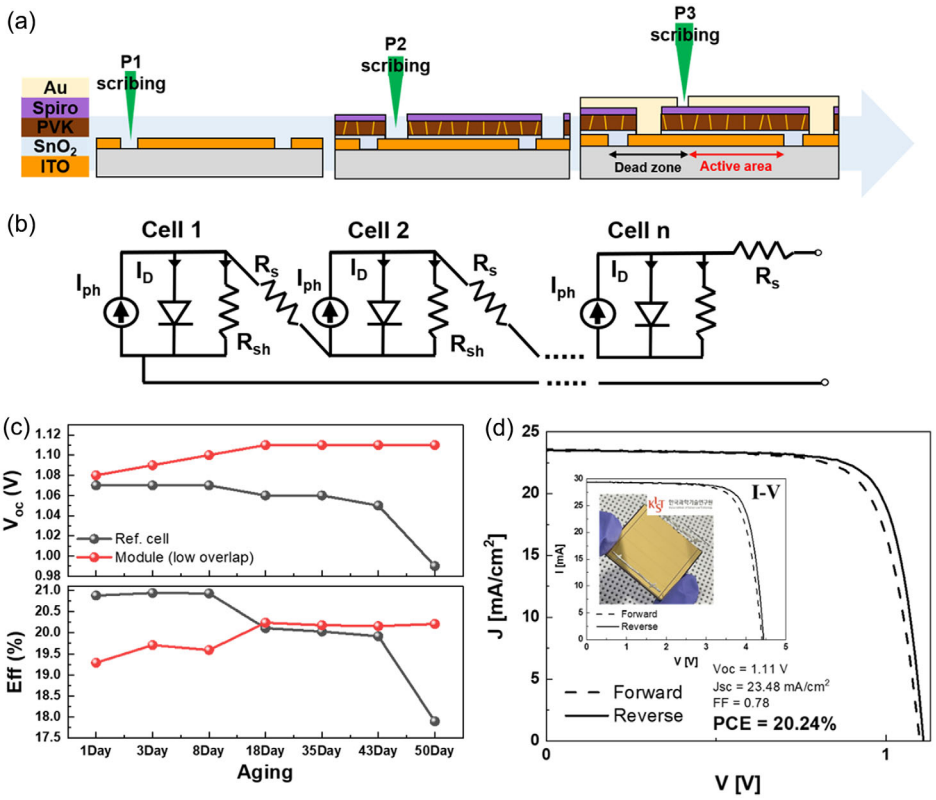


Figure 5. a) Fabrication process of perovskite solar module with all-laser-scribing (scribing steps is composed of P1–P2–P3). b) Equivalent circuit of monolithic interconnected module. (I_{ph}: photocurrent, I_D: diode current, R_s: series resistance, R_{sh}: shunt resistance). c) Comparison of efficiency and V_{OC} in reference cell and module by applying low-power and low-laser-overlap condition overtime. d) *J–V* curve of the best perovskite module using an optimized P3-scribing condition. The module efficiency is 20.24% (18 days aging). The active area of the module is 5 cm^2 and the inset is a photo of perovskite module.

thin ITO films. Further, the ns laser of visible 532 nm wavelength could efficiently trigger a nonlinear absorption process assisted by impurities in ITO as absorbing centers and thickness-wise uniform heating facilitated thermal stress-induced film removal.[56]

2) P2—after P1 laser scribing, the SnO_2 (electron-transport layer; ETL), perovskite (absorber layer), and spiro-OMeTAD (hole-transport layer; HTL) layers were sequentially spin-coated, and the P2 laser scribing removed a stack of ETL/absorber layer/HTL layers, which exposes the ITO bottom electrode so that the exposed ITO could electrically contact the Au top electrode upon subsequent Au deposition. A ps laser of 532 nm wavelength (selectively absorbing perovskite) was used for the delicately selective thin-film removal tasks. However, it is important that P2 scribing removes ETL (e.g., SnO_2) with minimal damage to the ITO; otherwise, the excessive series resistance decreases the module efficiency.[22] The main challenge in this context is the low absorption selectivity between SnO_2 and ITO, and the strong adhesion between SnO_2 and ITO.[57,58] Clearly, further improvement is necessary in the future; however, the abovementioned P2-scribing process has allowed the evaluation of the optimal P3-scribing condition at the module level.

2) P3–P3 scribing was performed after Au top-electrode deposition for isolation at the top-electrode level.

In the previous section, we studied the effect of laser scribing only on PSCs and not on modules. We applied an optimized P3 laser overlap condition to the perovskite module and observed the device performance and stability to have the same effect on the perovskite module. The design of the fabricated module is seen in Figure S11, Supporting Information. Based on the previous results, 0.05 W; 0.08 J cm^{-2} with a fast scan speed of 2 m s^{-1} was considered the best condition. Therefore, we applied this condition to module fabrication and compared its device characteristics with those of a reference cell. The reference PSC was fabricated under the same conditions as the module without laser processing. Figure 5c shows the V_{OC} and efficiency variations of the reference cell and perovskite module under the optimized P3 conditions as a function of time (all *J–V* curves and device characteristics overtime are shown in Figure S16 and Table S2, Supporting Information, respectively). The perovskite modules show an increase in V_{OC} and efficiency overtime up to 50 days, but a decrease in efficiency after very long aging (5 months) (see Figure S17, Supporting Information). There are two possible reasons for the difference in efficiency between modules and cells. First, in the module, the entire sample is covered with Au electrodes, whereas in the cell only the electrode area is covered. Thus, oxygen or moisture penetrates more easily through relatively open regions, which is considered to be worse

© 2024 Wiley-VCH GmbH

2367198x, 2024, 8, Downloaded from https://onlinelibrary.wiley.com/doi/10.1002/solr.202301040 by Ewha Womans University Library, Wiley Online Library on [10/11/2024]. See the Terms and Conditions (https://onlinelibrary.wiley.com/terms-and-conditions) on Wiley Online Library for rules of use; OA articles are governed by the applicable Creative Commons License

Table 3. Measured device parameters of perovskite module (active area: 5 cm^2).

	V_{OC} [V]	J_{SC} [mA cm^{-2}]	I_{SC} [mA]	FF [%]	Eff [%]
For (0 day)	4.25 (1.06)[a)]	5.90 (23.60)[b)]	29.50	73.07	18.32
Rev (0 day)	4.31 (1.08)[a)]	5.88 (23.52)[b)]	29.40	76.23	19.29
For (18 days aging)	4.40 (1.10)[a)]	5.89 (23.56)[b)]	29.45	74.74	19.35
Rev (18 days aging)	4.45 (1.11)[a)]	5.87 (23.48)[b)]	29.35	77.62	20.24

[a)]The value was derived by dividing the V_{OC} of the module by its cell number. [b)]J_{SC} per single cell was determined by dividing the I_{SC} with single cell area.

for long-term stability. Second, improved stability can be due to the laser-scribing effect. We displayed several modules and cell aging data in Supporting Information. As shown in Figure S18b, Supporting Information, the stability of cell with laser scribing under low-power and low-overlap conditions (yellow plot) is slightly improved compared to cells without laser scribing. Because of these two factors, the perovskite modules are assumed to be more stable than that of cells.

The superior stability of perovskite module can be explained by the fact that there is no direct perovskite illumination or heating that could cause degradation or damage to the perovskite layer, under low-overlap conditions compared to reference cell. The reference cell exhibited a gradual decrease in V_{OC} and efficiency as the sample is aged. Based on these experiments, we successfully fabricated a perovskite mini-module with an efficiency of 20.24% (18 days aging) in an active area of 5 cm^2. The *J–V* curve is shown in Figure 5d (**Table 3**).

3. Conclusion

This study investigated the effect of P3-laser-scribing parameters on scribing line shapes and material removal, and their roles in device performance and stability in PSCs. Our results demonstrate an improvement in V_{OC} and stability when employing low-overlap laser conditions (e.g., high scanning speed of 2 m s^{-1}), regardless of the laser power. Even after 2 months, the efficiency of the cell maintains 90% of its initial efficiency when using optimized P3-laser-scribing conditions. The extent of the laser overlap determines the degree of exposure and damage to the perovskite material, which affects the stability of the device. Through PL and TEM/EDX measurements, we showed that a reduced laser overlap led to more PbI_2 formation on the processed surface compared with high-overlap conditions. This contributed to the enhancement of the V_{OC} of perovskite solar module. In this study, we successfully achieved a perovskite minimodule with an efficiency of 20.24%. We believe that this study highlights the importance of the laser processing parameters in perovskite modules and contributes to achieving high-efficiency solar modules.

4. Experimental Section

Materials: N,N-dimethylformamide (DMF, Sigma-Aldrich, anhydrous, 99.8%), dimethyl sulfoxide (DMSO, Sigma-Aldrich, anhydrous, ≥99.9%), chlorobenzene (Sigma-Aldrich, anhydrous, 99.8%), bis(trifluoromethane)sulfonimide lithium salt (Sigma-Aldrich, 99.95% trace metals basis), acetonitrile (Sigma-Aldrich, anhydrous, 99.8%), methyl acetate (Sigma-Aldrich, anhydrous, 99.5%), rubidium iodide (RbI, Sigma-Aldrich, 99.9% trace metals basis), and lead(II) bromide ($PbBr_2$, Sigma-Aldrich, ≥98%) were purchased from Sigma-Aldrich. Formamidinium iodide (FAI, Greatsolar, >99.99%), methylammonium bromide (MABr, Greatsolar, >99.99%), and methylammonium chloride (MACl, Greatsolar, >99.99%) were purchased from Greatcell Solar Materials. Lead(II) iodide (PbI_2, 99.9985% metal basis) was purchased from Thermos Scientific.

Fabrication of PSC: Our devices used ITO (HANALINTECH) as the bottom electrode with a thickness of 150 nm and a sheet resistance of 10 Ω sq^{-1}. These substrates were subjected to ultrasonic cleaning in the following order: Deconex, acetone, deionized water, and Isopropyl alcohol (IPA). After cleaning, these substrates were dried in the oven at 70 °C. The substrates were exposed to the O_2 plasma (HARRICK PLASMA, PDC-002-HP) for 15 min before SnO_2 coating. A 3.75 wt% SnO_2 colloidal nanoparticle water-based solution was spin-coated (Dong Ah Trade, ACE-200) on ITO glass at 4000 rpm for 30 s and annealed at 150 °C for 30 min to deposit the SnO_2 layer. Further, a 1.5 M double-cation perovskite $(FA_{0.95}MA_{0.05})Pb(I_{0.95}Br_{0.05})_3$ precursor solution was prepared with DMF and a DMSO solvent (8:1 volume ratio). Subsequently, RbI (5 mol%) and MACl (35 mol% of MACl were added to the solution. This solution was spin-coated (Dong Ah Trade, ACE-200) onto the SnO_2 layer at 4000 rpm for 30 s. During spin-coating, methyl acetate was dripped as an anti-solvent and the films were annealed at 155 °C. After cooling down, spiro-OMeTAD was spin-coated (Dong Ah Trade, ACE-200) at 6000 rpm for 60 s. The spiro-OMeTAD solution was prepared in chlorobenzene (72 mg mL^{-1}) and doped with 17.5 µL bis(trifluoromethane)sulfonimide lithium salt (520 mg mL^{-1} in acetonitrile), and 28.8 µL 4-tert-butylpyridine. Finally, 70 nm of Au was deposited using a thermal evaporator (Korea Vacuum Tech, KVE-T2000).

P3-Scribing Test on PSCs: P3 scribing was performed on the Au electrode of PSCs. The scribed lines were situated at the center of the black mask for measurement (see detailed schematic images in Figure S19, Supporting Information). The active area defined by the mask was 0.07 cm^2. The laser focal spot diameter of ≈14 µm (1/e definition) was observed on sample surface, as experimentally measured using the Gaussian fitting process based on features generated by various laser power levels.[59] The nominal pulse-to-pulse overlap calculated based on the measured beam diameter in 1/e definition, (1—beam diameter/scanning speed × laser firing frequency) × 100 (%), was 44%, 17%, and <1% for the scanning speeds of 1, 1.5, and 2 m s^{-1}, respectively (note that the pulse-to-pulse overlap could be varied due to slight changes in beam size with power).

Fabrication of Perovskite Solar Module and Laser Scribing: The lasers used in the experiment were a ps laser (Advanced Optowave, AOPICO) and an ns laser (Spectraphysics, HIPPO). Glass covered with 150 nm thick ITO (ITO glass) substrates was first cleaned in the same way as the cells to fabricate the perovskite solar module. After cleaning, P1 scribing was performed. The 532 nm wavelength ns laser with a frequency of 20 kHz was used for P1 scribing. The P1 processing conditions included a laser power of 0.7 W, scanning speed of 50 mm s^{-1}, and Defocus (DF) of 1 mm were used. Further, it was processed into two lines with an overlap of 0.01 mm. After P1 scribing, the substrates were cleaned in an ultrasonicator using IPA and dried in the oven at 70 °C. SnO_2 /perovskite/spiro-OMeTAD was coated in the same manner as the cells after the substrates were dried. Subsequently, P2 scribing was performed using a 532 nm wavelength ps laser with a laser frequency of 100 kHz. The P2 processing conditions included a laser power of 0.2 W and a scanning speed of 250 mm s^{-1}. It was processed into three lines with an overlap of 0.01 mm. Further, samples were then deposited by Au using a thermal evaporator in the high vacuum chamber (≈10^{-6} mTorr) until the Au was 70 nm. Finally, P3

© 2024 Wiley-VCH GmbH

2367198x, 2024, 8, Downloaded from https://onlinelibrary.wiley.com/doi/10.1002/solr.202301040 by Ewha Womans University Library, Wiley Online Library on [10/11/2024]. See the Terms and Conditions (https://onlinelibrary.wiley.com/terms-and-conditions) on Wiley Online Library for rules of use; OA articles are governed by the applicable Creative Commons License

scribing was performed using the same laser as in P2 scribing (the laser power and scanning speed were different). All laser-scribing processes were performed on the film side using a circular beam.

Fabrication of PSC and Characterization: Current density–voltage (*J–V*) characteristics were measured in ambient air under 1.5 G illumination using a Keithley 2400 source meter. The scan range was from −0.2 to +1.2 V for both reverse and forward scans. Surface and cross-sectional OM, SEM, and TEM images of the P3 processing region were obtained using Olympus BX53M, Regulus8230, and FEI Tecnai G2 F20 X-TWIN, respectively. For TEM measurements, lamellar samples were prepared via a focused ion beam (FIB, Helios G4 HX). Rough milling was performed with an acceleration voltage of 30 kV and current of 2.4 nA, and fine milling was performed with an acceleration voltage of 30 kV and a current of 90 pA. The sampling for TEM was performed with an acceleration voltage of 5 kV and a current of 63 pA. In this experiment, we used a gun voltage of 200 kV with an emission current of ≈115 μA, dwell time of 5 μs pixel^{-1}, and 140e nm^{-2} of electron does. Under this condition, we have not seen critical sample damage during the measurement.

PL Mapping Measurements: PL measurements, which include spatial mapping, were performed using a McPherson 207 spectrometer equipped with a thermoelectric (TE)-cooled charge-coupled-device array detector (Andor Newton DU940P-BV) and a modified microscope (Olympus BX51M). The grating had 150 grooves mm^{-1} and was blazed to 500 nm. A perovskite layer was excited by a 457 nm diode-pumped solid-state laser focused to ≈1 μm by a 100X microscope objective lens. Further, we used the excitation energy of 2.71 eV (457 nm) because the bandgap of perovskite was measured to be 1.58–1.59 eV by the external quantum efficiency (EQE) measurements and that of PbI_2 was reported to be 2.2–2.3 eV.[60,61] The incident laser power was 10 μW for minimizing light-induced change in the sample. A step size of 1 μm was applied for PL mapping to distinguish regions of different patterning conditions because the shape of the P3 line was different with respect to patterning laser power and exposure velocity. The average size of scanned area was ≈40 × 30 μm^2 for PL mapping.

Supporting Information

Supporting Information is available from the Wiley Online Library or from the author.

Acknowledgements

This work was supported by the Technology Development Program to Solve Climate Changes through the National Research Foundation (NRF) funded by the Ministry of Science, ICT (grant nos. 2019M1A2A2072412 and 2022M3J1A1085373) of the Republic of Korea and KIST Institutional Program. This work was supported by the Basic Science Research Program (grant nos. NRF-2022R1A2C1010497 and NRF-2018R1A6A1A03025340) through the National Research Foundation of Korea (NRF).

Conflict of Interest

The authors declare no conflict of interest.

Data Availability Statement

The data that support the findings of this study are available from the corresponding author upon reasonable request.

Keywords

cell-to-module losses, laser scribings, monolithic integrated modules, perovskite solar cells

Received: December 14, 2023
Revised: March 22, 2024
Published online: April 4, 2024

[1] H. J. Snaith, *Nat. Mater.* **2018**, *17*, 372.
[2] Best Research-Cell Efficiency Chart | Photovoltaic Research | NREL, https://www.nrel.gov/pv/cell-efficiency.html.
[3] T. H. Le, H. Driscoll, C. H. Hou, A. Montgomery, W. Li, J. S. Stein, W. Nie, *Adv. Electron. Mater.* **2023**, *9*, 2300093.
[4] D. B. Ritzer, T. Abzieher, A. Basibüyük, T. Feeney, F. Laufer, S. Ternes, B. S. Richards, S. Bergfeld, U. W. Paetzold, *Prog. Photovolt. Res. Appl.* **2022**, *30*, 360.
[5] Z. Bi, X. Xu, X. Chen, Y. Zhu, C. Liu, H. Yu, Y. Zheng, P. A. Troshin, A. Guerrero, G. Xu, *Chem. Eng. J.* **2022**, *446*, 137164.
[6] Z. Liang, S. Zhang, X. Xu, N. Wang, J. Wang, X. Wang, Z. Bi, G. Xu, N. Yuan, J. Ding, *RSC Adv.* **2015**, *5*, 60562.
[7] K. Hwang, Y. S. Jung, Y. J. Heo, F. H. Scholes, S. E. Watkins, J. Subbiah, D. J. Jones, D. Y. Kim, D. Vak, *Adv. Mater.* **2015**, *27*, 1241.
[8] A. T. Mallajosyula, K. Fernando, S. Bhatt, A. Singh, B. W. Alphenaar, J. C. Blancon, W. Nie, G. Gupta, A. D. Mohite, *Appl. Mater. Today* **2016**, *3*, 96.
[9] S. Razza, F. Di Giacomo, F. Matteocci, L. Cinà, A. L. Palma, S. Casaluci, P. Cameron, A. D'Epifanio, S. Licoccia, A. Reale, T. M. Brown, A. Di Carlo, *J. Power Sources* **2015**, *277*, 286.
[10] T. Bu, L. K. Ono, J. Li, J. Su, G. Tong, W. Zhang, Y. Liu, J. Zhang, J. Chang, S. Kazaoui, F. Huang, Y. B. Cheng, Y. Qi, *Nat Energy* **2022**, *7*, 528.
[11] J. W. Yoo, J. Jang, U. Kim, Y. Lee, S. G. Ji, E. Noh, S. Hong, M. Choi, S. I. Seok, I. L., *Joule* **2021**, *5*, 2420.
[12] S. Chen, X. Dai, S. Xu, H. Jiao, L. Zhao, J. Huang, *Science* **2021** *373*, 902.
[13] H. Wang, Z. Qin, Y. Miao, Y. Zhao, *Trans. Tianjin Univ.* **2022**, *28*, 323.
[14] N. G. Park, K. Zhu, *Nat. Rev. Mater.* **2020**, *5*, 333.
[15] D. Castro, V. C. M. Duarte, L. Andrade, *ACS Omega* **2022**, *7*, 40844.
[16] L. Gao, L. Chen, S. Huang, X. Li, G. Yang, *ACS Appl. Energy Mater.* **2019**, *2*, 3851.
[17] S. M. P. Meroni, K. E. A. Hooper, T. Dunlop, J. A. Baker, D. Worsley, C. Charbonneau, T. M. Watson, *Energies* **2020**, *13*, 1589.
[18] A. L. Palma, *Solar RRL.* **2020**, *4*, 1900432.
[19] A. L. Palma, F. Matteocci, A. Agresti, S. Pescetelli, E. Calabrò, L. Vesce, S. Christiansen, M. Schmidt, A. Di Carlo, *IEEE J. Photovolt.* **2017**, *7*, 1674.
[20] K. G. Brooks, M. K. Nazeeruddin, *Adv. Energy Mater.* **2021**, *11*, 2101149.
[21] L. Rakocevic, R. Gehlhaar, T. Merckx, W. Qiu, U. W. Paetzold, H. Fledderus, J. Poortmans, *IEEE J. Photovolt.* **2017**, *7*, 404.
[22] M. Yang, D. H. Kim, T. R. Klein, Z. Li, M. O. Reese, B. J. Tremolet De Villers, J. J. Berry, M. F. A. M. Van Hest, K. Zhu, *ACS Energy Lett.* **2018**, *3*, 322.
[23] X. Dai, S. Chen, Y. Deng, A. Wood, G. Yang, C. Fei, J. Huang, *PRX Energy* **2022**, *1*, 013004.
[24] D. Castro, V. C. M. Duarte, L. Andrade, *ACS Omega* **2022**, *7*, 40844.
[25] X. Wang, M. Ehrhardt, P. Lorenz, C. Scheit, S. Ragnow, X. W. Ni, K. Zimmer, *Appl. Surf. Sci.* **2014**, *302*, 194.
[26] B. Taheri, F. De Rossi, G. Lucarelli, L. A. Castriotta, A. Di Carlo, T. M. Brown, F. Brunetti, *ACS Appl. Energy Mater.* **2021**, *4*, 4507.

© 2024 Wiley-VCH GmbH

2367198x, 2024, 8, Downloaded from https://onlinelibrary.wiley.com/doi/10.1002/solr.202301040 by Ewha Womans University Library, Wiley Online Library on [10/11/2024]. See the Terms and Conditions (https://onlinelibrary.wiley.com/terms-and-conditions) on Wiley Online Library for rules of use; OA articles are governed by the applicable Creative Commons License

[27] C. Schultz, M. Fenske, J. Dagar, A. Zeiser, A. Bartelt, R. Schlatmann, E. Unger, B. Stegemann, *Sol. Energy.* **2020**, *198*, 410.
[28] Y. Galagan, *J. Phys. Energy.* **2020**, *2*, 021004.
[29] F. U. Kosasih, L. Rakocevic, T. Aernouts, J. Poortmans, C. Ducati, *ACS Appl. Mater. Interfaces* **2019**, *11*, 45646.
[30] Z. Li, T. R. Klein, D. H. Kim, M. Yang, J. J. Berry, M. F. A. M. Van Hest, K. Zhu, *Nat. Rev. Mater.* **2018**, *3*, 18017.
[31] M. Fenske, C. Schultz, J. Dagar, F. U. Kosasih, A. Zeiser, C. Junghans, A. Bartelt, C. Ducati, R. Schlatmann, E. Unger, B. Stegemann, *Energy Technol.* **2021**, *9*, 2000969.
[32] Y. Gao, H. Raza, Z. Zhang, W. Chen, Z. Liu, *Adv. Funct. Mater.* **2023**, *33*, 2215171.
[33] G. Li, X. Zou, J. Cheng, X. Bai, D. Chen, Y. Yao, C. Chang, X. Yu, Z. Zhou, J. Wang, B. Liu, *Mater. Lett.* **2020**, *273*, 127979.
[34] L. Wang, C. McCleese, A. Kovalsky, Y. Zhao, C. Burda, *J. Am. Chem. Soc.* **2014**, *136*, 12205.
[35] Y. Hu, E. M. Hutter, P. Rieder, I. Grill, J. Hanisch, M. F. Aygüler, A. G. Hufnagel, M. Handloser, T. Bein, A. Hartschuh, K. Tvingstedt, V. Dyakonov, A. Baumann, T. J. Savenije, M. L. Petrus, P. Docampo, *Adv. Energy. Mater.* **2018**, *8*, 1703057.
[36] P. Yadav, M. I. Dar, N. Arora, E. A. Alharbi, F. Giordano, S. M. Zakeeruddin, M. Grätzel, *Adv. Mater.* **2017**, *29*, 1701077.
[37] N. Ueoka, T. Oku, A. Suzuki, *AIP Adv.* **2020**, *10*, 125023.
[38] I. J. Park, S. Seo, M. A. Park, S. Lee, D. H. Kim, K. Zhu, H. Shin, J. Y. Kim, *ACS Appl. Mater. Interfaces* **2017**, *9*, 41898.
[39] S. Jeong, S. S. Ham, E. P. Choi, D. J. Hwang, H. Yu, W. M. Kim, G. Y. Kim, J. Jeong, *ACS Appl. Energy Mater.* **2023**, *6*, 3745.
[40] Edward D. Palik, *Handbook of Optical Constants of Solids*, Academic Press, Orlando, USA **1997**.
[41] W. Benxin, Y. C. Shin, *Appl. Surf. Sci.* **2009**, *255*, 4996.
[42] W. Benxin, Y. C. Shin, Shin, *Appl. Surf. Sci.* **2007**, *253*, 4079.
[43] P. P. Pronko, S. K. Dutta, D. Du, R. K. Singh, *J Appl. Phys.* **1995**, *78*, 6233.
[44] G. E. Norman, S. V. Starikov, V. V. Stegailov, *J. Exp. Theor. Phys.* **2012**, *114*, 792.
[45] S. Preuss, A. Demchuk, M. Stuke, *Appl. Phys.* **1995**, *61*, 33.
[46] Y. Cheng, Y. Peng, A. K. Y. Jen, H. L. Yip, *Sol. RRL* **2022**, *6*, 2100545.
[47] S. Kuk, Z. Wang, H. Yu, C. Y. Nam, J.-H. Jeong, D. Hwang, *Prog. Photovolt. Res. Appl.* **2020**, *28*, 135.
[48] H. Han, X. Jia, C. Ma, Y. Wu, *Sol. Energy Mater. Sol. Cells* **2022**, *240*, 111714.
[49] K. Zimmer, X. Wang, P. Lorenz, L. Bayer, M. Ehrhardt, C. Scheit, A. Braun, *Phys. Procedia* **2014**, *56*, 1024.
[50] Y. Chen, Q. Meng, Y. Xiao, X. Zhang, J. Sun, C. B. Han, H. Gao, Y. Zhang, Y. Lu, H. Yan, *ACS Appl. Mater. Interfaces* **2019**, *11*, 44101.
[51] B. Shi, X. Yao, F. Hou, S. Guo, Y. Li, C. Wei, Y. Ding, Y. Li, Y. Zhao, X. Zhang, *J. Phys. Chem. C* **2018**, *122*, 21269.
[52] G. Tumen-Ulzii, C. Qin, D. Klotz, M. R. Leyden, P. Wang, M. Auffray, T. Fujihara, T. Matsushima, J. W. Lee, S. J. Lee, Y. Yang, C. Adachi, *Adv. Mater.* **2020**, *32*, 1905035.
[53] F. Liu, Q. Dong, M. K. Wong, A. B. Djurišić, A. Ng, Z. Ren, Q. Shen, C. Surya, W. K. Chan, J. Wang, A. M. C. Ng, C. Liao, H. Li, K. Shih, C. Wei, H. Su, J. Dai, *Adv. Energy Mater.* **2016**, *6*, 1502206.
[54] M. Zhong, S. Zhang, L. Huang, J. You, Z. Wei, X. Liu, J. Li, *Nanoscale* **2017**, *9*, 3736.
[55] R. Frisenda, J. O. Island, J. L. Lado, E. Giovanelli, P. Gant, P. Nagler, S. Bange, J. M. Lupton, C. Schüller, A. J. Molina-Mendoza, L. Aballe, M. Foerster, T. Korn, M. Angel Niño, D. P. De Lara, E. M. Pérez, J. Fernandéz-Rossier, A. Castellanos-Gomez, *Nanotechnology* **2017**, *28*, 455703.
[56] S. Kuk, Z. Wang, S. Fu, T. Zhang, Y. Y. Yu, J. Choi, J. H. Jeong, D. J. Hwang, *Appl. Phys. Lett.* **2018**, *112*, 134102.
[57] Z. Wang, S. Kuk, B. Kang, P. Lee, J.-H. Jeong, D. J. Hwang, *Appl. Surf. Sci* **2020**, *505*, 144408.
[58] L. Rakocevic, G. Schöpe, B. Turan, J. Genoe, T. Aernouts, S. Haas, R. Gehlhaar, J. Poortmans, *Prog. Photovolt. Res. Appl.* **2020**, *28*, 1120.
[59] J. M. Liu, *Opt. Lett.* **1982**, *7*, 196.
[60] R. Frisenda, J. O. Island, J. L. Lado, E. Giovanelli, P. Gant, P. Nagler, S. Bange, J. M. Lupton, C. Schüller, A. J. Molina-Mendoza, L. Aballe, M. Foerster, T. Korn, M. Angel Niño, D. P. De Lara, E. M. Pérez, J. Fernandéz-Rossier, A. Castellanos-Gomez, *Nanotechnology* **2017**, *28*, 455703.
[61] Z. Y. Wu, B.-L. Jian, H.-C. Hsu, *Opt. Mater. Express* **2019**, *9*, 1882.

© 2024 Wiley-VCH GmbH

2367198x, 2024, 8, Downloaded from https://onlinelibrary.wiley.com/doi/10.1002/solr.202301040 by Ewha Womans University Library, Wiley Online Library on [10/11/2024]. See the Terms and Conditions (https://onlinelibrary.wiley.com/terms-and-conditions) on Wiley Online Library for rules of use; OA articles are governed by the applicable Creative Commons License